Research article

Yan-Hong Zhou, Shaohui Yu, Yuejun Li, Xin Luo, Xiaohong Zheng* and Lei Zhang*

Pure spin current generation with photogalvanic effect in graphene interconnect junctions

https://doi.org/10.1515/nanoph-2020-0646
Received December 7, 2020; accepted February 21, 2021; published online March 12, 2021

Abstract: We investigate the photovoltaic behaviors of magnetic graphene interconnect junctions, which are constructed by zigzag graphene nanoribbons (ZGNRs), with the aim to produce pure spin current by photogalvanic effect (PGE). Two kinds of interconnect junctions are designed by connecting two 6-ZGNR with a carbon hexagon (C6) and a carbon tetragon (C4), respectively. It is found that zero charge current is produced under irradiation of light in both structures due to the presence of spatial inversion symmetry. Nevertheless, behind the zero charge current, net pure spin current is produced in the structure with a C6, but not in the structure with a C4. This difference originates from their different edge state distribution and different spatial inversion symmetry of the spin density. However, interestingly, local edge pure spin current can be obtained in both structures. More importantly, the pure spin current generation is independent of the photon energy, polarization type or polarization angle, suggesting a robust way of generating pure spin current with PGE and new possibility of graphene's applications in spintronics.

Keywords: density functional theory; graphene; photon; pure spin current; spintronics.

***Corresponding authors**: **Xiaohong Zheng**, College of Science, East China Jiao Tong University, Nanchang, Jiangxi 330013, China; Key Laboratory of Materials Physics, Institute of Solid State Physics, HFIPS, Chinese Academy of Sciences, Hefei 230031, China; and State Key Laboratory of Quantum Optics and Quantum Optics Devices, Institute of Laser Spectroscopy, Shanxi University, Taiyuan 030006, China; and **Lei Zhang**, State Key Laboratory of Quantum Optics and Quantum Optics Devices, Institute of Laser Spectroscopy, Shanxi University, Taiyuan 030006, China; and Collaborative Innovation Center of Extreme Optics, Shanxi University, Taiyuan 030006, China, E-mail: xhzheng@theory.issp.ac.cn (X. Zheng), zhanglei@sxu.edu.cn (L. Zhang). https://orcid.org/0000-0002-3027-1042 (X. Zheng)
Yan-Hong Zhou, **Yuejun Li and Xin Luo**, College of Science, East China Jiao Tong University, Nanchang, Jiangxi 330013, China
Shaohui Yu, School of Mathematics and Statistics, Hefei Normal University, Hefei 230061, China

1 Introduction

The field of two dimensional (2D) materials has been rapidly expanding in recent years and has drawn intensive research attention due to their exceptional mechanical, electronic and optoelectronic properties, providing promising building blocks for future nanoelectronic and photoelectronic devices [1–14]. Although graphene is the first successfully fabricated 2D material and has been studied for nearly two decades, it has always been the object of numerous studies all the years [15–26]. Especially, a number of research studies in graphene have been extended to the field of spintronics in recent years [19, 20, 27–31], and many novel spin and magnetic properties such as tunnel magnetoresistance, spin polarized transport, spin switching effects and pure spin current have been reported [15, 18–20, 22, 26, 32, 33], suggesting the great potential of graphene in spintronic devices. In particular, pure spin current, which is a central topic in spintronics and characterized by the opposite flow directions of electrons of different spins with equal magnitude, is rather interesting due to its low energy consumption characteristics and thus has received intensive attention. By far, several mechanisms for generating spin currents in graphene have already been proposed, such as spin–orbit coupling [32], quantum Hall effect [33] and Andreev reflection in structures with normal-superconductor boundaries [22]. Actually, new mechanisms for producing pure spin current are still an interesting topic in the study of graphene.

It is well known that another striking feature of this one-atom-thick material is that it provides a good candidate for constructing all-carbon circuits by proper patterning or etching on it, just as proposed by Areshkin and White [34]. Obviously, any such all-carbon circuit eventually consists of nanostructured units such as nanoribbons that are engineered from graphene. These structures present distinctly different electronic and transport properties [35]. For example, the structures with armchair edges are nonmagnetic while those with zigzag edges are magnetic. They may behave as semiconductors or metals, depending on their edge shape and edge size.

Open Access. ©2021 Yan-Hong Zhou et al., published by De Gruyter. This work is licensed under the Creative Commons Attribution 4.0 International License.

However, most previous studies were focused on their one-dimensional forms [35–40]. As a matter of fact, in the design of nanoelectronic circuits, the formation of interconnects where two nanoribbons combine together is unavoidable [34] and they will necessarily introduce scatterings when electrons pass through them. Such scatterings are the physics basis of a working device and thus the interconnects themselves at the atomic scale may also work as electronic and optoelectronic devices. More importantly, the transport behaviors of interconnects may greatly differ from the purely one-dimensional forms and dominate in the performance of the nanoelectronic circuits [41, 42]. Moreover, new functions can be achieved by combining two graphene nanoribbons. For example, robust half-metallic transport [42] and definitive spin switches [43] can be realized by connecting two zigzag graphene nanoribbons (ZGNRs) with a carbon tetragon. In SiC nanoribbon interconnects, perfect spin and valley polarized transport is achieved [41]. Such functional units greatly extend the versatility and applicability of graphene nanoribbons and other 2D materials in real applications.

On the other hand, the current through a device can be generated not only by an electrical bias, but also by light irradiation through photovoltaic effect. The latter driving force of current provides not only ways of fully utilizing solar energy, but also ways of realizing goals that are not achievable by an electrical bias in many materials. For example, pure spin current has been achieved by light irradiation in traditional semiconductors [44]. With the rise of molecular electronics and nanoelectronics, intensive attention has also been paid to exploiting the photovoltaic effect in molecular and nanoscale devices to realize various goals [45–53]. From these previous studies, we know that for systems with spatial inversion symmetry, a finite detectable photocurrent is generated when a small auxiliary bias voltage is applied across the device to induce electronic asymmetry [46–48]. More interestingly, in systems lacking a center of inversion symmetry, the photocurrent can be generated even without an applied auxiliary bias voltage, which is known as the photogalvanic effect (PGE) [49–53]. Since its first discovery in 1978 in traditional semiconductors [49, 50], PGE has been attracting increasing attention [54–61] and lots of striking transport properties induced by PGE, such as spin-galvanic effect [62], photoexcitation of pure valley-orbit currents [63], photo-spin-voltaic effect [63, 64] and so on, have been found. In recent years, the research interest has been extended to devices constructed with low dimensional materials, especially 2D materials, such as phospherene [65], MoS_2 [66], SiC [67], silicene [68], etc.

In this work, we investigate the photovoltaic behaviors of graphene interconnects. Specifically, we consider two typical kinds of interconnects which are formed by connecting two identical ZGNRs with a carbon hexagon (C6) and a carbon tetragon (C4), respectively. Both structures have anti-ferromagnetic zigzag edges and spatial inversion symmetry. We intend to investigate that for these graphene interconnects, what will be their photoresponses and especially, whether they are able to produce pure spin current by PGE. It is found that zero charge current is produced under irradiation of light in both structures if a finite bias is absent due to spatial inversion symmetry in them. However, interestingly, behind the zero charge current, pure spin current is produced in the structure with a C6, but not in the structure with a C4. This difference arises from their different spatial inversion symmetry of the spin density. More importantly, the pure spin current in the C6 system with spatial inversion symmetry is independent of the photon energy, polarization type or polarization angle. This is in clear contrast to the schemes with PGE in phospherene and SiC nanoribbons where pure spin current can only be realized at certain specific polarization angle or special photon energy [68, 69]. Consequently, the interconnects with a C6 provide perfect candidates for robustly producing pure spin current with PGE.

2 Simulation model and computational details

The two-probe photovoltaic devices are junctions constructed by connecting the up-right and down-left corners of two 6-ZGNRs which contain six carbon zigzag chains along the longitude direction, as shown in Figure 1(a). We consider two kinds of connection styles that have been reported in the literature [42, 43]. In the first style, the two nanoribbons are connected by a C6 ring (hexagon) and can be well developed either by a mechanical etching technique [70] or by rational bottom-up synthesis based on single molecular precursors [71–73], while in the second one, they are connected by a C4 ring (tetragon), which can be prepared using a bottom-up self-assembly synthesis technique on a reconstructed Au template [43, 74]. For simplicity, the two devices are called 'Junction C6' and 'Junction C4', respectively. The C6 and C4 rings are indicated by the red circles in Figure 1(b) and (c). Each edge carbon atom is passivated by one hydrogen atom to saturate the dangling bond since without hydrogen passivation, the edges with dangling bonds are not stable and tend to be reconstructed, with two consecutive hexagons transformed into one heptagon and one pentagon

[75, 76]. The nanoribbons prepared by a bottom-up synthesis method are naturally hydrogenated [71, 72]. Each device is divided into three parts: the left electrode (left), the right electrode (right) and the central region (central), which are shown in Figure 1. In each junction, the central region consists of two parts taken from the two nanoribbons and each part contains 5.5 unit cells, with a length of 12.298 Å and a width of 11.360 Å as measured between edge carbon atoms. One unit cell with a length of 2.46 Å and a width of 11.360 Å is chosen to perform bulk calculations of the leads. In this way, both structures satisfy the spatial inversion symmetry. A supercell with a vacuum of more than 10 Å is chosen in the x and y directions, so that the actual lattice vectors for the central region are chosen as $36.0 \times 14.0 \times 28.285$ Å for the C6 structure and $36.0 \times 14.0 \times 25.31$ for the C4 structure, along the x, y and z directions, respectively, which are large enough to keep the device from any interaction with its periodic images in the transverse directions.

Light, with the photon energy $\hbar\omega$, is normally shed on the whole central region in the y direction. **A** is the light electromagnetic vector potential in the xz plane and θ/ϕ is the polarization (helicity) angle of the linearly (elliptically) polarized light. The electronic structure and photovoltaic transport properties are calculated by the first-principles quantum transport package NanoDcal which combines the density-functional theory (DFT) and the non-equilibrium Greens function (NEGF) technique [77–79]. Norm-conserving pseudopotentials are used to describe the atomic cores and a double zeta plus polarization (DZP) basis is adopted for electron wave functions of carbon and hydrogen atoms, and the convergence criterion for Hamiltonian and electron density is 1×10^{-8} in atomic units. The exchange–correlation potential is treated at the level of generalized gradient approximation with the form of Perdew, Burke, and Ernzerhof [80]. Moreover, a Monkhorst–Pack k-mesh of $1 \times 1 \times 150$ (for the leads) and a cutoff energy of 150 Ry are chosen to achieve a balance between calculation efficiency and accuracy. The structure relaxations are performed with a force tolerance of 0.02 eV/Å.

The photocurrent from the central region to each lead is calculated in a post-processing way. Firstly, the self-consistent Hamiltonians of the leads and the central region are obtained by DFT or DFT-NEGF calculations, without taking into account the electron–photon interaction. With these self-consistent Hamiltonians, the retarded (advanced) Green's function G_0^r (G_0^a) of the central region. Then the electron–photon interaction $\frac{q}{m}p \cdot \mathbf{A}$ where $\mathbf{p}$ is the electron momentum included in the calculation of the

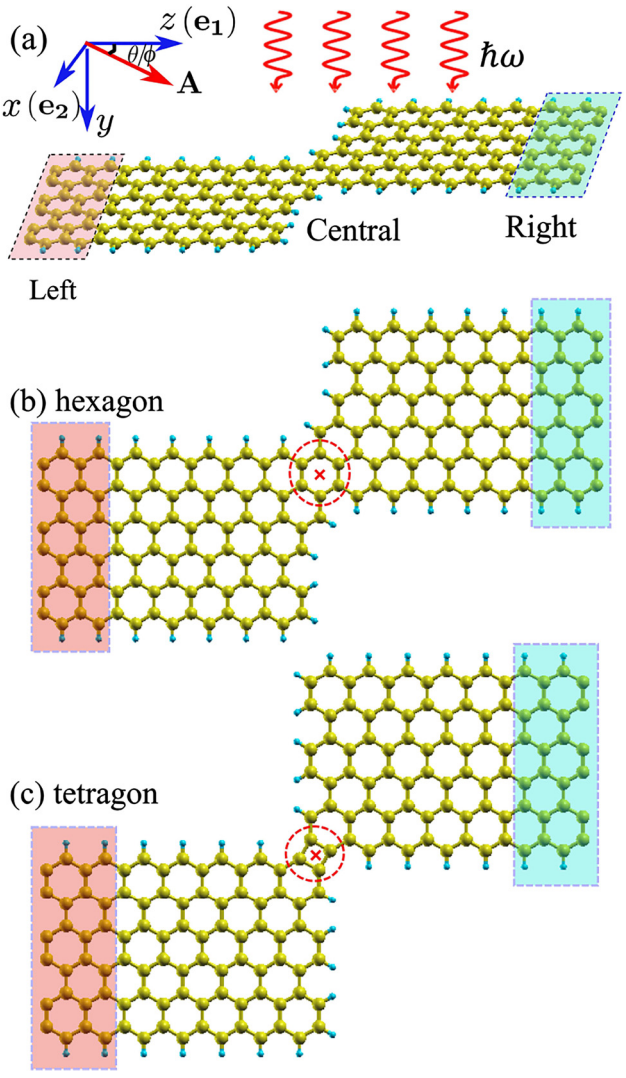

Figure 1: (a) The photovoltaic junction model constructed with two 6-ZGNRs interconnected at two corners. (b) The top view of Junction C6 with a hexagon at the connection; (c) the top view of Junction C4 with a tetragon at the connection. Light is normally incident to the xz plane. $\mathbf{e_1} = \hat{z}$ and $\mathbf{e_2} = \hat{x}$ are two polarized vectors that determine the incident direction of the polarized light. The red spiral arrows denote the applied polarized light. **A** is the electromagnetic vector potential and θ/ϕ is the polarization/helicity angle of the linearly/elliptically polarized light. The red circle indicates the hexagon or tetragon at the connection. The red cross in the circle indicates the spatial inversion center of the device.

lesser (greater) Green's function of the central region by $G_{\mathrm{ph}}^{<(>)} = G_0^r[\Sigma_{\mathrm{ph}}^{<(>)} + \Sigma_{\mathrm{L}}^{<(>)} + \Sigma_{\mathrm{R}}^{<(>)}]G_0^a$, where $\Sigma_\alpha^{r/a}$ is the self-energy of the semi-infinite lead α ($\alpha = (L, R)$) and $\Sigma_{\mathrm{ph}}^{</>}$ is the self-energy from the electron–photon interaction considered in the first-order Born approximation [81]. The effective transmission function is calculated by [66]

$$T_{\mathrm{eff},\alpha}(\varepsilon) = \mathrm{Tr}\{\Gamma_\alpha(\varepsilon)[(1 - f_\alpha(\varepsilon))G_{\mathrm{ph}}^<(\varepsilon) + f_\alpha(\varepsilon)G_{\mathrm{ph}}^>(\varepsilon)]\}, \quad (1)$$

where $\Gamma_\alpha = i(\Sigma_\alpha^r - \Sigma_\alpha^a)$ is the line-width function of the lead α describing the coupling between the central region and lead α, and f_α is the Fermi–Dirac distribution of the lead α. The spin-dependent photocurrent from the central region to the lead α is calculated by [66]

$$I_{\alpha,\sigma}^{\mathrm{ph}} = \frac{ie}{h}\int T_{\mathrm{eff},\alpha,\sigma}(\varepsilon)\mathrm{d}\varepsilon, \tag{2}$$

where $\sigma = (\uparrow, \downarrow)$ is the spin index. For the full details of the theoretical formalism, we refer to references [66, 81]. In practice, the normalized photocurrent, *i.e.*, the photoresponse function written as [65, 81]

$$R = \frac{I_{\alpha,\sigma}^{\mathrm{ph}}}{I_\omega} \tag{3}$$

is discussed for convenience where I_ω is the photon flux defined as the number of photons per unit time per unit area and the unit of R is a_0^2/photon.

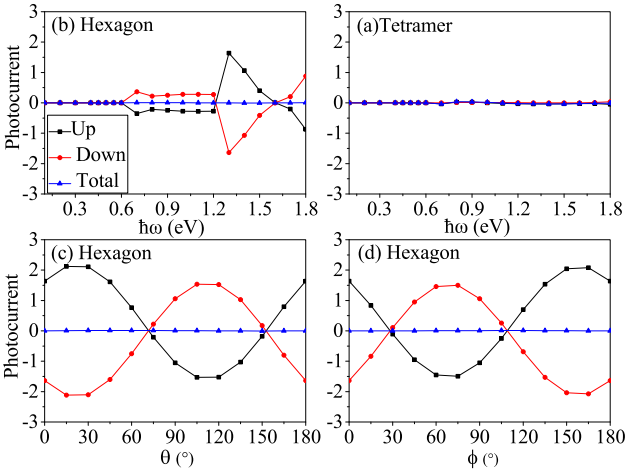

Figure 2: The spin dependent photocurrents of: (a) Junction C6 and (b) Junction C4 as a function of photon energy $\hbar\omega$ under linearly polarize light with polarization angle $\theta = 0^\circ$. The spin dependent photocurrents of Junction C6 as a function of: (c) polarization angle θ under linearly polarized light and (d) helicity angle ϕ under elliptically polarized light, with the photon energy taken as $\hbar\omega = 1.3$ eV as an example.

3 Results and discussion

At first, we study the photovoltaic effect of both Junction C6 and Junction C4 as shown in Figure 1, with the linearly polarized light irradiated on the whole central region. The spin dependent photocurrents for the two junctions as a function of photon energy $\hbar\omega$ at the polarization angle $\theta = 0^\circ$ are shown in Figure 2(a) and (b). For the two types of connection configurations, the photocurrent for either spin channel is zero when the photon energy is lower than the band gap (0.62 eV) of the 6-ZGNR since with photon energy below the band gap no electrons can be excited. When the photon energy exceeds 0.62 eV, the two junctions behave completely differently. For Junction C6, a rather large value is observed in both the spin up and spin down photocurrent components. In contrast, in Junction C4, both spin components are always negligible, which means unobservable photovoltaic effect in it. Most interesting is that, in Junction C6, the two spin components of the photocurrent are exactly equal in magnitudes but with opposite signs in the considered photon energy range (0.7, 1.8 eV). The opposite signs mean opposite flow directions of electrons in the two spin channels. Thus, the sum of the two spin components is always zero at any photon energy ($I_c = I_{up} + I_{down} = 0$), which means that there is no charge current across Junction C6, while the difference between the two spin components is nonzero ($I_s = I_{up} - I_{down} = 2I_{up}$), suggesting that finite pure spin current is produced. Next, for Junction C6, we further study the effect of the polarization/helicity angle θ/ϕ of the linearly/elliptically polarized light on the pure spin current generation by PGE by taking the photon energy $\hbar\omega = 1.30$ eV as an example. As shown in Figure 2(c), under the linearly polarized light, both the spin up and spin down photocurrents satisfy a sinusoid relation of $\pm a\sin(2\theta + \theta_0) \pm b$ where a, b and ϕ_0 are three device related parameters, and the two components always have the same magnitude and opposite flow directions in the polarization angle range from 0° to 180°. Thus, pure spin current is always achieved under the linearly polarized light irradiation with any polarization angle. Likewise, under the elliptically polarized light, a similar sinusoid relation of spin dependent photocurrents is obtained and we can also get pure spin current at any helicity angle ϕ, as clearly seen from Figure 2(d).

It is very surprising that the PGE induced pure spin current is so robust in Junction C6 in the sense that the pure spin current generation is independent of the optical setup parameters such as the photon energy, polarization type and polarization angle, but the two spin components of photocurrent are always negligible in Junction C4, if we take into consideration that both configurations have spatial inversion symmetry. In the following, we will understand this striking difference by comparing their electronic structures. To start with, the band structure of a single 6-ZGNR in the ground state is presented in Figure 3(a). It is found that the two spin channels are degenerate in energy. Thus, no difference can be seen just from the band structure. However, great difference in the two spin channels can be observed from inspecting the real space distribution of

the eigenstates. As an example, the states of the valence band and conduction band at the X point are shown in Figure 3(b). These are edge states. Actually, the states from the valence band maximum and conduction band minimum to the X points are all localized edge states (not shown). We focus on the edge states in the following discussions. In the spin up channel, the valence band states are localized at the upper edge while the conduction band states are localized at the lower edge. On the contrary, in the spin down channel, the valence band states are localized at the lower edge while the conduction band states are localized at the upper edge. Since only the valence bands are filled by electrons, it leads to the opposite magnetic moments on the two edges, thus the edge states on the two edges are antiferromagnetically coupled in the ground state. In addition, the coupling between any two nearest neighboring atoms belonging to two sublattices A and B is always antiferromagnetic due to the spin alteration rule [82, 83], which can be seen from sign alteration of the atomic magnetic moment with the order of 0.29, −0.05, 0.08, −0.04, 0.04, −0.03, 0.03, −0.04, 0.04, −0.08, 0.05, and −0.29 μ_B in the unit cell when it goes from one edge to the other.

When we combine two 6-ZGNRs either by a C6 or a C4 ring, all the carbon atoms are sp^2 hybridized and the spin alteration rule has to be still satisfied. Thus, the atomic magnetic moments represented by the spin density will look like those shown in Figure 4. Consequently, in Junction C6, in both the left and right ribbons, the positive edge magnetic moments are at the upper edge and the negative edge magnetic moments are at the lower edge. In contrast, in Junction C4, in the left ribbon, the positive edge magnetic moments are at the upper edge and the negative magnetic moments are at the lower edge, while in the right ribbon, the positions of the positive and negative atomic magnetic moments are exchanged. Deducing from these facts, we will see that for both junctions, in the left lead, the spin up (down) valence edge state is localized at the

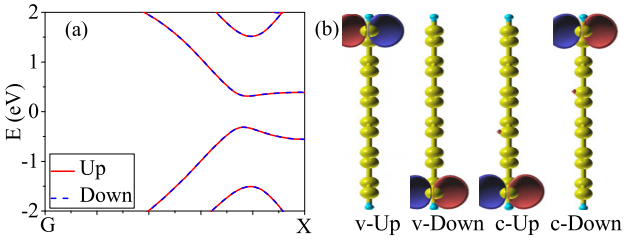

Figure 3: (a) The band structure of 6-ZGNR in the ground state; (b) the real space distribution of the edge states in the valence band (v) and the conduction band (c) at the X point. 'Up' and 'Down' mean spin up and spin down components, respectively.

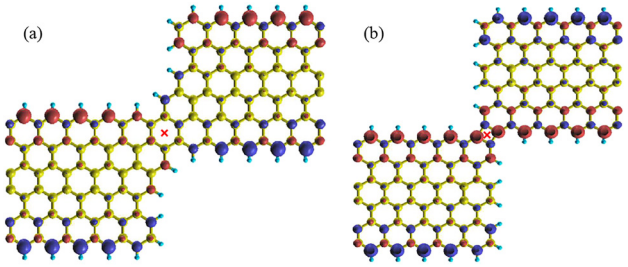

Figure 4: The real space distribution of spin density of: (a) Junction C6; (b) Junction C4. The red cross indicates the spatial inversion center of the device. It is clearly seen that the spin density in Junction C6 is anti-symmetrical with respect to the spatial inversion center while it is symmetrical in Junction C4.

upper (lower) edge while the spin up (down) conduction edge state is localized at the lower (upper) edge, as shown by the schematic plots in Figure 5(a)–(d). However, the situations for the right leads of the two junctions are completely different. To be specific, for Junction C6, the spin up (down) valence edge state is localized at the upper (lower) edge and the spin up (down) conduction edge state is localized at the lower (upper) edge (see Figure 5(a) and (b)). In contrast, for Junction C4, the spin up (down) valence edge state is localized at the lower (upper) edge and the spin up (down) conduction edge state is localized at the upper (lower) edge (see Figure 5(c) and (d)).

From the edge state distributions in real space, we can analyze the excitation processes of electrons under light irradiation. The electrons can enter the central region from the valence bands of the left ribbon and go out from the conduction band of the right ribbon. Meanwhile, electrons can also enter from the valence bands of the right ribbon and go out from the conduction band of the left ribbon. (Here, the processes of entering and going out from the same lead may also happen but they are omitted due to their no contribution to any measurable current in this lead.) Both the left-to-right process and the right-to-left process can be further divided into two sub-processes according to the spin channels of the edge states. The sub-processes are plotted in Figure 5.

We first look at Junction C6. Due to spin matching, there are two left-to-right processes indicated by 'P_1' for spin up channel going from the upper edge of the left lead to the lower edge of the right lead and 'P_2' for spin down channel from the lower edge of the left lead to the upper edge of the right lead (see Figure 5(a)). Likewise, there are two right-to-left processes indicated by 'P_3' for spin down channel from the lower edge of the right lead to the upper edge of the left lead and 'P_4' for spin up channel from the upper edge of the right lead to the lower edge of the left

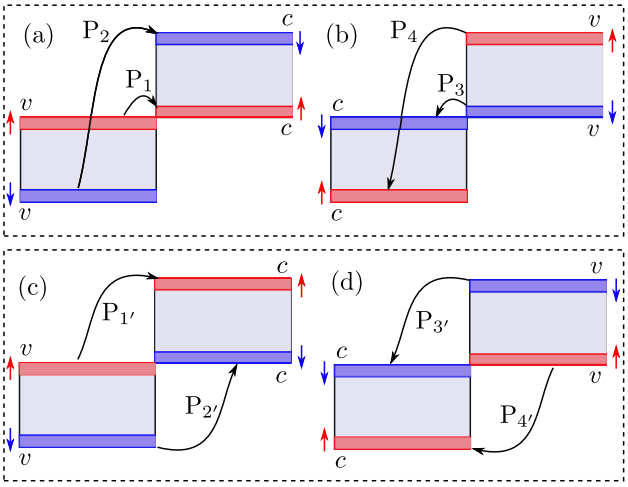

Figure 5: The schematic model of electron excitation processes: (a) and (b) for Junction C6; (c) and (d) for Junction C4. The red and blue narrow rectangles indicate the positions of the spin up and spin down edge states, respectively. v means valence band while c means conduction band. The bent arrows indicate the possible excitation paths as marked by $P_1(P_{1'})$, $P_2(P_{2'})$, $P_3(P_{3'})$ and $P_4(P_{4'})$. For example, P_1 means that in Junction C6, electrons are excited from the spin up valence band edge states at the upper edge of the left ribbon to the spin up conduction band edge states at the lower edge of the right ribbon.

lead (see Figure 5(b)). Since the spin up valence edge state in the left lead is exactly the same as the spin down valence edge state in the right lead and the spin up conduction edge state in the right lead is exactly the same as the spin down conduction edge state in the left lead, processes 'P_1' and 'P_3' will have exactly the same magnitude. For the same reason, 'P_2' and 'P_4' will also have the same magnitude. The two processes 'P_1' and 'P_3' will contribute a right flowing pure spin current while 'P_2' and 'P_4' will contribute a left flowing pure spin current. Thus, these two pure spin currents will cancel partly, but not fully since the spatial separation between the initial and final edge states in processes 'P_1' and 'P_3' is much smaller than that in 'P_2' and 'P_4' and thus the electrons in 'P_1' and 'P_3' experience much smaller scattering than those in 'P_2' and 'P_4'. Eventually, the pure spin current produced by 'P_1' and 'P_3' will dominate.

We now turn to Junction C4. There are also two left-to-right processes indicated by '$P_{1'}$' for spin up channel going from the upper edge of the left lead to the upper edge of the right lead and '$P_{2'}$' for spin down channel from the lower edge of the left lead to the lower edge of the right lead (see Figure 5(c)). In the meantime, there are two right-to-left processes '$P_{3'}$' for spin down channel going from the upper edge of the right lead to the upper edge of the left lead and '$P_{4'}$' for spin up channel from the lower edge of the right lead to the lower edge of the left lead (see Figure 5(d)). Different from Junction C6, the spatial separations between the initial valence edge state and the final conduction edge state are the same for all these processes, which means that the scattering experienced by the electrons in all the four processes will be the same. Thus, the contributions from the four processes will be equal in magnitude. Considering the opposite flow directions, '$P_{1'}$' will cancel out with '$P_{4'}$' for spin up channel and '$P_{2'}$' will cancel out with '$P_{3'}$' for spin down channel. This leads to basically zero total current for each spin channel in each lead. That is what we see in Figure 2(b), where the very small deviations from zero arise from numerical errors in the computation. However, we note that, although both the total spin up and spin down photocurrents are zero for each lead, pure spin current can still be locally detected everywhere at the edges since the two counteracting (right moving and left moving) processes for each spin channel are localized at different edges (occurring at the upper and lower edges simultaneously in both leads). If we focus on the two processes occurring at the upper edge, we will see it very clearly since the spin up '$P_{1'}$' flows right while spin down '$P_{3'}$' flows left, which contribute to right flowing pure spin current at the upper edges in the two leads. Likewise, at the lower edges, there will be a left flowing pure spin current contributed by processes '$P_{2'}$' and '$P_{4'}$'. Such locally hidden pure spin currents are not reflected in the total spatially integrated pure spin current for each lead shown in Figure 2(b) and the observation depends on the progress of local detection technique. As a matter of fact, the local detection of edge spin current can be well performed by low-temperature scanning Kerr rotation microscopy which is capable of spatial/local imaging of the spin Hall effect [84].

Finally, the robustness of finite pure spin current in Junction C6 and zero pure spin current in Junction C4 is determined by the anti-symmetrical and symmetrical spin density in real space. For anti-symmetrical spin density, the potential barrier experienced by electrons of one spin channel in one direction will be exactly the same as that of the other spin channel in the opposite direction. Meanwhile, the potential barrier experienced by electrons in each spin channel will be different along two opposite directions. Thus, we can always get photocurrent with opposite directions and equal magnitude for the two spin channels, which leads to pure spin current. However, in Junction C4, the spin density is symmetrical with respect to the inversion center, which means that the potential barriers experienced by electrons in each spin channel will be the same along any two opposite directions. Consequently,

the total photocurrent for each spin channel in each lead will be zero.

4 Summary

Based on first-principles transport calculations, we have investigated the photovoltaic effect of two kinds of graphene nanoribbon interconnects constructed with two identical ZGNRs with six zigzag carbon chains along the longitudinal direction. Junction C6 has a hexagon while Junction C4 has a tetragon at the connection interfaces. Both junctions have spatial inversion symmetry, thus both present the same charge transport behavior under light irradiation, namely zero total charge current. However, it is found that the connection differences between the two nanoribbons lead to strikingly different spin-dependent photovoltaic effect and it arises from the different edge state distributions in real space in the two junctions. In particular, in Junction C6, finite total pure spin current can be robustly generated, neither dependent on the photon energy, nor dependent on the polarization type or polarization angle of the applied polarized light. In contrast, in Junction C4, both vanishing total charge current and total pure spin current will be produced. The results can be well understood by a cartoon model represented by four processes occurring between the edge states in the two ribbons. The findings suggest new possibilities of graphene's application in spintronic devices.

Acknowledgement: This work was supported by the National Natural Science Foundation of China (Nos. 61764005, 11804093, 11974355, 11704232 and 12074230), the Natural Science Foundation of Jiangxi Province (Nos. 20181BAB201013 and 20202ACBL212005), the Natural Science Foundation of Jiangxi Provincial Education Department, China (No. GJJ180324), National Key R&D Program of China under Grant No. 2017YFA0304203, the Natural Science Foundation of Jiangxi Provincial Education Department (No. GJJ180324), Shanxi Province 100-Plan Talent Program and 1331KSC, the Open Research Fund Program of the State Key Laboratory of Low-Dimensional Quantum Physics and the Program of State Key Laboratory of Quantum Optics and Quantum Optics Devices under Grant No. KF201810.

Author contribution: All the authors have accepted responsibility for the entire content of this submitted manuscript and approved submission.

Research funding: None declared.

Conflict of interest statement: The authors declare no conflicts of interest regarding this article.

References

[1] K. S. Novoselov, A. K. Geim, S. V. Morozov, et al., "Electric field effect in atomically thin carbon films," *Science*, vol. 306, p. 666, 2004.

[2] J. R. Schaibley, H. Yu, G. Clark, et al., "Valleytronics in 2D materials," *Nat. Rev. Mater.*, vol. 1, p. 16055, 2016.

[3] G. Eda and S. A. Maier, "Two-dimensional crystals: managing light for optoelectronics," *ACS Nano*, vol. 7, p. 5660, 2013.

[4] S. Z. Butler, S. M. Hollen, L. Cao, et al., "Progress, challenges, and opportunities in two-dimensional materials beyond graphene," *ACS Nano*, vol. 7, p. 2898, 2013.

[5] G. R. Bhimanapati, Z. Lin, V. Meunier, et al., "Recent advances in two-dimensional materials beyond graphene," *ACS Nano*, vol. 9, p. 11509, 2015.

[6] N. Sethulakshmi, A. Mishra, P. Ajayan, et al., "Magnetism in two-dimensional materials beyond graphene," *Mater. Today*, vol. 27, p. 107, 2019.

[7] C. R. Ryder, J. D. Wood, S. A. Wells, and M. C. Hersam, "Chemically tailoring semiconducting two-dimensional transition metal dichalcogenides and black phosphorus," *ACS Nano*, vol. 10, p. 3900, 2016.

[8] M. Long, P. Wang, H. Fang, and W. Hu, "Progress, challenges, and opportunities for 2D material based photodetectors," *Adv. Funct. Mater.*, vol. 29, p. 1803807, 2019.

[9] L. Kou, C. Chen, and S. C. Smith, "Phosphorene: fabrication, properties, and applications," *J. Phys. Chem. Lett.*, vol. 6, p. 2794, 2015.

[10] Y. Liu, X. Duan, Y. Huang, and X. Duan, "Two-dimensional transistors beyond graphene and TMDCs," *Chem. Soc. Rev.*, vol. 47, p. 6388, 2018.

[11] Y. Yoon, K. Ganapathi, and S. Salahuddin, "How good can monolayer MoS_2 transistors be?," *Nano Lett.*, vol. 11, p. 3768, 2011.

[12] H. Liu, A. T. Neal, Z. Zhu, et al., "Phosphorene: an unexplored 2D semiconductor with a high hole mobility," *ACS Nano*, vol. 8, p. 4033, 2014.

[13] F. A. Rasmussen and K. S. Thygesen, "Computational 2D materials database: electronic structure of transition-metal dichalcogenides and oxides," *J. Phys. Chem. C*, vol. 119, p. 13169, 2015.

[14] M. Topsakal, S. Cahangirov, E. Bekaroglu, and S. Ciraci, "First-principles study of zinc oxide honeycomb structures," *Phys. Rev. B*, vol. 80, p. 235119, 2009.

[15] Z. P. Niu, "Tunnel anisotropic magnetoresistance in graphene with Rashba spin–orbit interaction," *J. Phys. Condens. Matter*, vol. 23, p. 435302, 2011.

[16] L. Razzaghi and M. V. Hosseini, "Quantum transport of Dirac fermions in graphene with a spatially varying Rashba spin–orbit coupling," *Phys. E Low-dimens. Syst. Nanostruct.*, vol. 72, p. 89, 2015.

[17] M. M. Wysokiński and J. Spałek, "Seebeck effect in the graphene-superconductor junction," *J. Appl. Phys.*, vol. 113, p. 163905, 2013.

[18] A. Dyrdał, J. Barnaś, and V. Dugaev, "Current-induced spin polarization in graphene due to Rashba spin–orbit interaction," *Phys. Rev. B*, vol. 89, p. 075422, 2014.

[19] R. Mohammadkhani, B. Abdollahipour, and M. Alidoust, "Strain-controlled spin and charge pumping in graphene

devices via spin-orbit coupled barriers,'' *Europhys. Lett.*, vol. 111, p. 67005, 2015.
[20] K. Halterman, O. T. Valls, and M. Alidoust, ''Spin-controlled superconductivity and tunable triplet correlations in graphene nanostructures,'' *Phys. Rev. Lett.*, vol. 111, p. 046602, 2013.
[21] M. Salehi, M. Alidoust, Y. Rahnavard, and G. Rashedi, ''Thermal transport properties of graphene-based ferromagnetic/singlet superconductor/ferromagnetic junctions,'' *J. Appl. Phys.*, vol. 107, p. 123916, 2010.
[22] D. Greenbaum, S. Das, G. Schwiete, and P. Silvestrov, ''Pure spin current in graphene normal-superconductor structures,'' *Phys. Rev. B*, vol. 75, p. 195437, 2007.
[23] M. Salehi, M. Alidoust, and G. Rashedi, ''Signatures of d-wave symmetry on thermal Dirac fermions in graphene-based F|I|d junctions,'' *J. Appl. Phys.*, vol. 108, p. 083917, 2010.
[24] X.-F. Wang and T. Chakraborty, ''Collective excitations of Dirac electrons in a graphene layer with spin-orbit interactions,'' *Phys. Rev. B*, vol. 75, p. 033408, 2007.
[25] D. Zhang, Z. Bao, J. Su, C. Tang, C. Zang, and Y. Zhang, ''Thermal transport in four-terminal graphene nano-junctions,'' *Phys. B Condens. Matter*, vol. 407, p. 4333, 2012.
[26] J. Wang, L. Zhang, and K. S. Chan, ''Tunneling conductance of a magnetized zigzag graphene nanoribbon/superconductor junction,'' *Phys. Rev. B*, vol. 83, p. 125425, 2011.
[27] J. Hirsch, ''Spin Hall effect,'' *Phys. Rev. Lett.*, vol. 83, p. 1834, 1999.
[28] M. Alidoust and K. Halterman, ''Long-range spin-triplet correlations and edge spin currents in diffusive spin–orbit coupled SNS hybrids with a single spin-active interface,'' *J. Phys. Condens. Matter*, vol. 27, p. 235301, 2015.
[29] K. Halterman and M. Alidoust, ''Josephson currents and spin-transfer torques in ballistic SFSFS nanojunctions,'' *Supercond. Sci. Technol.*, vol. 29, p. 055007, 2016.
[30] M. Alidoust and K. Halterman, ''Spontaneous edge accumulation of spin currents in finite-size two-dimensional diffusive spin–orbit coupled SFS heterostructures,'' *New J. Phys.*, vol. 17, p. 033001, 2015.
[31] R. Raimondi, C. Gorini, M. Dzierzawa, and P. Schwab, ''Current-induced spin polarization and the spin Hall effect: a quasiclassical approach,'' *Solid State Commun.*, vol. 144, p. 524, 2007.
[32] C. L. Kane and E. J. Mele, ''Quantum spin Hall effect in graphene,'' *Phys. Rev. Lett.*, vol. 95, p. 226801, 2005.
[33] D. A. Abanin, P. A. Lee, and L. S. Levitov, ''Spin-filtered edge states and quantum Hall effect in graphene,'' *Phys. Rev. Lett.*, vol. 96, p. 176803, 2006.
[34] D. A. Areshkin and C. T. White, ''Building blocks for integrated graphene circuits,'' *Nano Lett.*, vol. 7, p. 3253, 2007.
[35] Y.-W. Son, M. L. Cohen, and S. G. Louie, ''Energy gaps in graphene nanoribbons,'' *Phys. Rev. Lett.*, vol. 97, p. 216803, 2006.
[36] Y. W. Son, M. L. Cohen, and S. G. Louie, ''Half-metallic graphene nanoribbons,'' *Nature*, vol. 444, p. 347, 2006.
[37] X. H. Zheng, I. Rungger, Z. Zeng, and S. Sanvito, ''Effects induced by single and multiple dopants on the transport properties in zigzag-edged graphene nanoribbons,'' *Phys. Rev. B*, vol. 80, p. 235426, 2009.
[38] E.-J. Kan, Z. Li, J. Yang, and J. G. Hou, ''Half-Metallicity in Edge-Modified Zigzag Graphene Nanoribbons,'' *J. Am. Chem. Soc.*, vol. 130, p. 4224, 2008.
[39] S. Dutta, A. K. Manna, and S. K. Pati, ''Intrinsic half-metallicity in modified graphene nanoribbons,'' *Phys. Rev. Lett.*, vol. 102, p. 096601, 2009.
[40] X. H. Zheng, R. N. Wang, L. L. Song, Z. X. Dai, X. L. Wang, and Z. Zeng, ''Impurity induced spin filtering in graphene nanoribbons,'' *Appl. Phys. Lett.*, vol. 95, p. 123109, 2009.
[41] X. Zheng, X. Chen, L. Zhang, L. Xiao, and S. Jia, ''Perfect spin and valley polarized quantum transport in twisted SiC nanoribbons,'' *2D Mater.*, vol. 4, p. 025013, 2017.
[42] L. Song, S. Jin, P. Jiang, H. Hao, X. Zheng, and L. Zhang, ''Realizing robust half-metallic transport with chemically modified graphene nanoribbons,'' *Carbon*, vol. 141, p. 676, 2019.
[43] P. Cui, Q. Zhang, H. Zhu, et al., ''Carbon tetragons as definitive spin switches in narrow zigzag graphene nanoribbons,'' *Phys. Rev. Lett.*, vol. 116, p. 026802, 2016.
[44] X. Tao, P. Jiang, H. Hao, X. Zheng, L. Zhang, and Z. Zeng, ''Pure spin current generation via photogalvanic effect with spatial inversion symmetry,'' *Phys. Rev. B*, vol. 102, p. 081402, 2020.
[45] X. Tao, L. Zhang, X. Zheng, et al., ''h-BN/graphene van der Waals vertical heterostructure: a fully spin-polarized photocurrent generator,'' *Nanoscale*, vol. 10, p. 174, 2018.
[46] P. Zhao, J. Li, W. Wei, et al., ''Giant anisotropic photogalvanic effect in a flexible AsSb monolayer with ultrahigh carrier mobility,'' *Phys. Chem. Chem. Phys.*, vol. 19, p. 27233, 2017.
[47] F. Chu, M. Chen, Y. Wang, et al., ''A highly polarization sensitive antimonene photodetector with a broadband photoresponse and strong anisotropy,'' *J. Mater. Chem. C*, vol. 6, p. 2509, 2018.
[48] T. Wang, M. Chen, B. Fan, et al., ''First-principles calculation of photocurrent in monolayer silicene sheet under small voltages,'' *Optic Commun.*, vol. 395, p. 289, 2017.
[49] E. L. Ivchenko and G. E. Pikus, ''New photogalvanic effect in gyrotropic crystals,'' *JETP Lett. (Engl. Transl.)*, vol. 27, p. 604, 1978.
[50] V. I. Belinicher and B. I. Sturman, ''The photogalvanic effect in media lacking a center of symmetry,'' *Sov. Phys. Usp.*, vol. 23, p. 415, 1980.
[51] S. D. Ganichev, E. L. Ivchenko, S. N. Danilov, et al., ''Conversion of spin into directed electric current in quantum wells,'' *Phys. Rev. Lett.*, vol. 86, p. 4358, 2001.
[52] C. Jiang, V. A. Shalygin, V. Y. Panevin, et al., ''Helicity-dependent photocurrents in graphene layers excited by midinfrared radiation of a CO_2 laser,'' *Phys. Rev. B*, vol. 84, p. 125429, 2011.
[53] M. Eginligil, B. Cao, Z. Wang, et al., ''Dichroic spin–valley photocurrent in monolayer molybdenum disulphide,'' *Nat. Commun.*, vol. 6, p. 7636, 2015.
[54] P. Král, E. J. Mele, and D. Tománek, ''Photogalvanic effects in heteropolar nanotubes,'' *Phys. Rev. Lett.*, vol. 85, p. 1512, 2000.
[55] X. W. He, B. Shen, Y. H. Chen, et al., ''Anomalous photogalvanic effect of circularly polarized light incident on the two-dimensional electron gas in Al{*x*}Ga{1 – *x*}N/GaN

heterostructures at room temperature,'' *Phys. Rev. Lett.*, vol. 101, p. 147402, 2008.
[56] A. G. Mal'shukov, ''Equilibrium circular photogalvanic effect in a hybrid superconductor-semiconductor system,'' *Phys. Rev. Lett.*, vol. 107, p. 146603, 2011.
[57] Y. Gao, Y. Zhang, and D. Xiao, ''Tunable layer circular photogalvanic effect in twisted bilayers,'' *Phys. Rev. Lett.*, vol. 124, p. 077401, 2020.
[58] S. Dhara1, E. J. Mele, and R. Agarwal, ''Voltage-tunable circular photogalvanic effect in silicon nanowires,'' *Science*, vol. 349, p. 726, 2015.
[59] S.-Y. Xu, Q. Ma, H. Shen, et al., ''Electrically switchable Berry curvature dipole in the monolayer topological insulator WTe_2,'' *Nat. Phys.*, vol. 14, p. 900, 2018.
[60] H. Yuan, X. Wang, B. Lian, et al., ''Generation and electric control of spin-valley-coupled circular photogalvanic current in WSe_2,'' *Nat. Nanotechnol.*, vol. 9, p. 851, 2014.
[61] Z. Ji, G. Liu, Z. Addison, et al., ''Spatially dispersive circular photogalvanic effect in a Weyl semimetal,'' *Nat. Mater.*, vol. 18, p. 955, 2019.
[62] S. D. Ganichev, E. L. Ivchenko, V. V. Bel'kov, et al., ''Spin-galvanic effect,'' *Nature*, vol. 417, p. 153, 2002.
[63] J. Karch, S. A. Tarasenko, E. L. Ivchenko, et al., ''Photoexcitation of valley-orbit currents in (111)-oriented silicon metal-oxide-semiconductor field-effect transistors,'' *Phys. Rev. B*, vol. 83, p. 121312, 2011.
[64] D. Ellsworth, L. Lu, J. Lan, et al., ''Photo-spin-voltaic effect,'' *Nat. Phys.*, vol. 12, p. 861, 2016.
[65] Y. Xie, L. Zhang, Y. Zhu, L. Liu, and H. Guo, ''Photogalvanic effect in monolayer black phosphorus,'' *Nanotechnology*, vol. 26, p. 455202, 2015.
[66] L. Zhang, K. Gong, J. Chen, et al., ''Generation and transport of valley-polarized current in transition-metal dichalcogenides,'' *Phys. Rev. B*, vol. 90, p. 195428, 2014.
[67] J. Chen, L. Zhang, L. Zhang, et al., ''Photogalvanic effect induced fully spin polarized current and pure spin current in zigzag SiC nanoribbons,'' *Phys. Chem. Chem. Phys.*, vol. 20, p. 26744, 2018.
[68] P. Jiang, L. Kang, X. Tao, et al., ''Robust generation of half-metallic transport and pure spin current with photogalvanic effect in zigzag silicene nanoribbons,'' *J. Phys. Condens. Matter*, vol. 31, p. 495701, 2019.
[69] Y. Xie, M. Chen, Z. Wu, et al., ''Two-dimensional photogalvanic spin-battery,'' *Phys. Rev. Appl.*, vol. 10, p. 034005, 2018.
[70] X. Wang and H. Dai, ''Etching and narrowing of graphene from the edges,'' *Nat. Chem.*, vol. 2, p. 661, 2010.
[71] G. D. Nguyen, H.-Z. Tsai, A. A. Omrani, et al., ''Atomically precise graphene nanoribbon heterojunctions from a single molecular precursor,'' *Nat. Nanotechnol.*, vol. 12, p. 1077, 2017.
[72] D. J. Rizzo, G. Veber, J. Jiang, et al., ''Inducing metallicity in graphene nanoribbons via zero-mode superlattices,'' *Science*, vol. 369, p. 1597, 2020.
[73] Z. Xiao, C. Ma, W. Lu, et al., ''Ab initio investigation of the cyclodehydrogenation process for polyanthrylene transformation to graphene nanoribbons,'' *npj Comput. Mater.*, vol. 5, p. 1, 2019.
[74] J. Cai, P. Ruffieux, R. Jaafar, et al., ''Atomically precise bottom-up fabrication of graphene nanoribbons,'' *Nature*, vol. 466, p. 470, 2010.
[75] P. Koskinen, S. Malola, and H. Häkkinen, ''Self-passivating edge reconstructions of graphene,'' *Phys. Rev. Lett.*, vol. 101, p. 115502, 2008.
[76] Ç. Ö. Girit, J. C. Meyer, R. Erni, et al., ''Graphene at the edge: stability and dynamics,'' *Science*, vol. 323, p. 1705, 2009.
[77] J. Taylor, H. Guo, and J. Wang, ''Ab initiomodeling of quantum transport properties of molecular electronic devices,'' *Phys. Rev. B*, vol. 63, p. 245407, 2001.
[78] J. Maassen, M. Harb, V. Michaud-Rioux, Y. Zhu, and H. Guo, ''Quantum transport modeling from first principles,'' *Proc. IEEE*, vol. 101, p. 518, 2013.
[79] M. Brandbyge, J.-L. Mozos, P. Ordejón, J. Taylor, and K. Stokbro, ''Density-functional method for nonequilibrium electron transport,'' *Phys. Rev. B*, vol. 65, p. 165401, 2002.
[80] J. P. Perdew and K. B. M. Ernzerhof, ''Generalized gradient approximation made simple,'' *Phys. Rev. Lett.*, vol. 77, p. 3865, 1996.
[81] L. E. Henrickson, ''Nonequilibrium photocurrent modeling in resonant tunneling photodetectors,'' *J. Appl. Phys.*, vol. 91, p. 6273, 2002.
[82] J. A. Chan, B. Montanari, J. D. Gale, S. M. Bennington, J. W. Taylor, and N. M. Harrison, ''Magnetic properties of polymerized C60: the influence of defects and hydrogen,'' *Phys. Rev. B*, vol. 70, p. 041403, 2004.
[83] L. Brey, H. A. Fertig, and S. Das Sarma, ''Diluted graphene antiferromagnet,'' *Phys. Rev. Lett.*, vol. 99, p. 116802, 2007.
[84] V. Sih, R. Myers, Y. Kato, W. Lau, A. Gossard, and D. Awschalom, ''Spatial imaging of the spin Hall effect and current-induced polarization in two-dimensional electron gases,'' *Nat. Phys.*, vol. 1, p. 31, 2005.